

LOW-METALLICITY YOUNG CLUSTERS IN THE OUTER GALAXY. II. Sh 2-208

CHIKAKO YASUI^{1, 2}, NAOTO KOBAYASHI^{3, 4, 2}, MASAO SAITO^{5, 6}, AND NATSUKO IZUMI^{3, 2}

¹Department of Astronomy, Graduate School of Science, University of Tokyo, Bunkyo-ku, Tokyo 113-0033, Japan;
 ck.yasui@astron.s.u-tokyo.ac.jp

²Laboratory of Infrared High-resolution spectroscopy (LIH), Koyama Astronomical Observatory, Kyoto Sangyo University, Motoyama,
 Kamigamo, Kita-ku, Kyoto 603-8555, Japan

³Institute of Astronomy, School of Science, University of Tokyo, 2-21-1 Osawa, Mitaka, Tokyo 181-0015, Japan

⁴Kiso Observatory, Institute of Astronomy, School of Science, University of Tokyo, 10762-30 Mitake, Kiso-machi, Kiso-gun, Nagano
 397-0101, Japan

⁵Nobeyama Radio Observatory, 462-2 Nobeyama, Minamimaki-mura, Minamisaku-gun, Nagano 384-1305, Japan

⁶The Graduate University of Advanced Studies, (SOKENDAI), 2-21-1 Osawa, Mitaka, Tokyo 181-8588, Japan

Received 2016 January 21; accepted 2016 February 17; will be published in AJ

ABSTRACT

We obtained deep near-infrared images of Sh 2-208, one of the lowest-metallicity H II regions in the Galaxy, $[O/H] = -0.8$ dex. We detected a young cluster in the center of the H II region with a limiting magnitude of $K = 18.0$ mag (10σ), which corresponds to a mass detection limit of $\sim 0.2 M_{\odot}$. This enables the comparison of star-forming properties under low metallicity with those of the solar neighborhood. We identified 89 cluster members. From the fitting of the K -band luminosity function (KLF), the age and distance of the cluster are estimated to be ~ 0.5 Myr and ~ 4 kpc, respectively. The estimated young age is consistent with the detection of strong CO emission in the cluster region and the estimated large extinction of cluster members ($A_V \sim 4$ –25 mag). The observed KLF suggests that the underlying initial mass function (IMF) of the low-metallicity cluster is not significantly different from canonical IMFs in the solar neighborhood in terms of both high-mass slope and IMF peak (characteristic mass). Despite the very young age, the disk fraction of the cluster is estimated at only $27 \pm 6\%$, which is significantly lower than those in the solar metallicity. Those results are similar to Sh 2-207, which is another low-metallicity star-forming region close to Sh 2-208 with a separation of 12 pc, suggesting that their star-forming activities in low-metallicity environments are essentially identical to those in the solar neighborhood, except for the disk dispersal timescale. From large-scale mid-infrared images, we suggest that sequential star formation is taking place in Sh 2-207, Sh 2-208 and the surrounding region, triggered by an expanding bubble with a ~ 30 pc radius.

Subject headings: Galaxy: abundances — infrared: stars — open clusters and associations: general
 — protoplanetary disks — stars: formation — stars: pre-main sequence

1. INTRODUCTION

The study of young low-metallicity clusters is of great interest because they enable us to characterize the metallicity dependence of star formation processes, such as the initial mass function (IMF) and star formation efficiency. Also, the study of the disk fraction for young clusters can constrain the probability of planet formation. They also provide an opportunity to study star formation in the early universe and to understand the star formation process itself (Yasui et al. 2016). Although nearby dwarf galaxies, such as the Large Magellanic Cloud (LMC) and the Small Magellanic Cloud (SMC), have been the primary targets of such studies (e.g., Brandl et al. 1996), our Galaxy also harbors a variety of low-metallicity clusters that enable the study of such objects with unprecedented detail.

The thin disk of our Galaxy is known to have a metallicity gradient, lower in the outer Galaxy, as well as other spiral galaxies (Rudolph et al. 2006). Although the existence of the metallicity gradient in the inner Galaxy ($R_G \lesssim 8$ kpc) is still under debate, a trend toward low metallicity can generally be seen in the outer Galaxy (Bono et al. 2013). For the derivation of the metallicity, various kinds of objects are used, including B-type stars (e.g., Smartt et al. 2001), Cepheid (e.g. Luck et al. 2006), H II regions (e.g. Rudolph et al. 2006), and open

clusters (e.g., Yong et al. 2012). Among these objects, H II regions have been found over a wide range of Galactic radii beginning long ago through a variety of H α emission surveys, starting with the pioneering work by Sharpless (1953). Sharpless (1959) compiled a catalog of 313 H II regions that is comprehensive for north of decl. -27° , covering the galactic longitudes of 0–272 deg and 315–360 deg. The Galactocentric distance of the regions span from ~ 0 to 18 kpc (Russeil 2003; Foster & Brunt 2015). Considering that H II regions are excited by O- or B-type stars with very short lifetimes of ~ 20 Myr at most, a large number of them are star-forming regions ($\sim 70\%$, Blitz et al. 1982). Therefore, we selected seven H II regions with estimated low metallicity, $[O/H] \leq -0.5$ dex, in the literature to construct a sample of low-metallicity young clusters.

In a series of papers, we present observations regarding the properties of young, low-metallicity clusters. In the first paper (Yasui et al. 2016), we presented the results for Sh 2-207 (S207), which is an H II region with a ~ 2.5 arcmin radius in the second Galactic quadrant with a metallicity of -0.8 dex. In the western region of S207, we identified a young cluster with a ~ 1 arcmin radius (corresponding to 1.3 pc) and a limiting magnitude of $K_S = 19.0$ mag (10σ) that corresponds to a mass detection limit of $\lesssim 0.1 M_{\odot}$. The age and distance of the clus-

ter are estimated at 2–3 Myr and ~ 4 kpc, respectively. The observed K -band luminosity function (KLF) suggests that the underlying IMF of the cluster down to the detection limit is not significantly different from typical IMFs in the solar metallicity. Based on the fraction of stars with near-infrared (NIR) excesses, a low disk fraction ($<10\%$) in the cluster with the relatively young age is suggested (see also Yasui et al. 2010).

In this paper, we present the results for the second target, Sh 2-208 (S208), which is one of the lowest-metallicity star-forming regions in the Galaxy with $12 + \log(\text{O}/\text{H}) \leq 8$ (Rudolph et al. 2006). S208 is located ~ 10 arcmin southward of S207. The two clusters consist of an ideal pair for studying low-metallicity clusters because their proximity in on-sky position and identical metallicities suggest that they are in similar environments. The combination of the S207 and S208 clusters may enable a unique study of the evolution of IMF and other star formation parameters (e.g., disk fraction, which is strongly related to the formation rate of the protoplanetary disk) in low-metallicity environments.

This paper is organized as follows. Section 2 describes previous studies on S208 and its star-forming activities using *WISE* (*Wide-field Infrared Survey Explorer*) and 2MASS (Two Micron All Sky Survey) data. Section 3 describes Subaru MOIRCS (Multi-Object InfraRed Camera and Spectrograph) deep JHK_S images and data reduction. Section 4 describes the results for a star-forming cluster in S208. In Section 5, we discuss the implications for the basic cluster parameters, such as age, distance, IMF, and disk fraction. Finally, in Section 6, we discuss the formation of those clusters in the outer arm in the Galactic context.

2. Sh 2-208

In this section, the properties of the target star-forming region, S208, are summarized. In Table 1, we summarize the properties from previous works: the coordinate, distance, oxygen abundance, and metallicity. We also show NIR and mid-infrared (MIR) pseudocolor images of S208 in Figure 1.

2.1. Basic Properties from the Literature

S208 is located at $(l, b) = (151.2870^\circ, +1.9682^\circ)$ on the Galactic plane with coordinates of $(\alpha_{2000.0}, \delta_{2000.0}) = (04^{\text{h}}19^{\text{m}}32.92^{\text{s}}, +52^\circ58'41.6'')$ from SIMBAD⁷ (Wenger et al. 2000). It has an extended H II region traced by H α emission (Sharpless 1959) and radio continuum emission (Fich 1993). It also accompanies strong MIR emission that is detected with IRAS (IRAS 04156+5251 in the IRAS Point Source Catalog; Beichman et al. 1988). CO emission is reported in Blitz et al. (1982) and Wouterloot & Brand (1989). A star-forming cluster is identified by Bica et al. (2003) using 2MASS images, with the center of $(\alpha_{2000.0}, \delta_{2000.0}) = (04^{\text{h}}19^{\text{m}}33^{\text{s}}, +58^\circ52'42'')$ and the angular dimensions of $1.2'$. The photometric distance, which is determined from spectroscopic and photometric observations, is estimated to be $\simeq 9$ kpc on average for a probable dominantly exciting late O-type or early

B-type star⁸, GSC 03719-00517 (7.6 kpc by Moffat et al. 1979, 9.4 kpc by Chini & Wink 1984, 10.0 kpc by Lahulla 1985; see the blue plus in Figure 1). Assuming that the Galactocentric distance of the Sun is $R_\odot = 8.0$ kpc, then the distance corresponds to $R_G \simeq 16.5$ kpc. It should be noted that the distance from such early-type stars may not be accurate because the luminosity class cannot be easily identified for early-type stars. On the other hand, the kinematic distance of S208 is estimated at about 4 kpc based on observations of the H α radial velocity using a Fabry–Perot spectrometer (4.0 kpc by Wouterloot & Brand 1989, 4.1 kpc by Caplan et al. 2000), and from radial velocities of H I data by CGPS and ^{12}CO line data by FCRAO (4.4 kpc by Foster & Brunt 2015). In this case, the distance corresponds to $R_G \simeq 12$ kpc. Figure 2 shows a top view of the Galaxy with S208 and the spiral arms. The locations of S208, assuming the photometric distance and kinematic distance, are shown with the open circle and the filled circle, respectively, while the spiral arms are shown with different colors, e.g., red for the Norma–Cygnus (outer) arm. The figure shows that S208 is located beyond the outer arm in the case of photometric distance, whereas it is located around the outer arm in the case of the kinematic distance. Later, we will propose that the distance to this cluster is more likely 4 kpc based on KLF analysis, which is similar to the above kinematic distance.

Based on the Fabry–Perot observations, Caplan et al. (2000) measured several optical emission line fluxes in [O II] $\lambda\lambda 3726$ and 3729 , H β , [O III] $\lambda 5007$, [He I] $\lambda 5876$, and H α , for 36 H II regions including S208. Subsequently, Deharveng et al. (2000) derived the oxygen abundance (O/H), as well as the extinctions, electron densities and temperatures, and ionic abundances (O^+/H^+ , O^{++}/H^+ , and He^+/H^+). The estimated oxygen abundance of S208 is $12 + \log(\text{O}/\text{H}) = 8.00$. Rudolph et al. (2006) reanalyzed the elemental abundances of 117 H II regions with updated physical parameters. Among the H II regions, the oxygen abundance of S208 is estimated using the data of Caplan et al. (2000) to be $12 + \log(\text{O}/\text{H}) = 7.91^{+0.16}_{-0.26}$. This corresponds to the metallicity of $[\text{O}/\text{H}] \simeq -0.8$ dex assuming the solar abundance of $12 + \log(\text{O}/\text{H}) = 8.73$ (Asplund et al. 2009). The spatial distribution of the Galactic abundance using the spectroscopy of Cepheids (Luck et al. 2006) also suggests low metallicity ($\lesssim -0.5$ dex) in the outer Galaxy at a distance of $D \gtrsim 4$ kpc in the second quadrant, where S208 is located, although it should be noted that some recent studies suggest a relatively flat metallicity gradient at a Galactocentric distance of $R_G \geq 12$ kpc (e.g., Korotin et al. 2014).

2.2. Star-forming Activities

Before discussing the results of our deep NIR imaging with Subaru, we discuss the star-forming activities in S208 based on 2MASS (Skrutskie et al. 2006) NIR data and *WISE* (Wright et al. 2010) MIR data. Figure 1 shows a pseudocolor image of S208 with a field of view of $\sim 10' \times 10'$ and with the center at $(l, b) =$

⁷ This research has made use of the SIMBAD database, operated at the Centre de Données Astronomiques de Strasbourg, France.

⁸ The spectral type is estimated at B0V by Crampton et al. (1978) and Moffat et al. (1979), while it is estimated to be O9.5V by Chini & Wink (1984) and Lahulla (1985).

(151.29°, +1.97°) in the Galactic coordinates. The figure is produced by combining the 2MASS K_S -band (2.16 μm , blue), *WISE* band 1 (3.4 μm ; green), and *WISE* band 3 (12 μm ; red) images. We also show the 1.4 GHz radio continuum from the NRAO VLA Sky Survey (NVSS; Condon et al. 1998) with white contours. The 12 μm emission is mainly from PAH emission, tracing photodissociation regions around H II regions, whereas the radio continuum traces the photoionized H II region. The distributions of the 12 μm emission and radio continuum show that the H II region extends almost spherically with an approximately 1 arcmin radius. From the nearly perfect spherical shape centered on GSC 03719-00517, this late O-type or early B-type star should be the main exciting source of the H II region.

3. OBSERVATION AND DATA REDUCTION

3.1. Subaru MOIRCS JHK Imaging

Deep JHK_S -band images were obtained for each band with the 8.2m Subaru telescope equipped with a wide-field NIR camera and spectrograph, MOIRCS (Ichikawa et al. 2006; Suzuki et al. 2008). MOIRCS employs two 2K “HAWAII-2” imaging arrays, which yield a $4' \times 7'$ field of view ($3.5' \times 4'$ for each chip) with a pixel scale of $0''.117 \text{ pixel}^{-1}$. The instrument uses the MKO NIR photometric filters (Simons & Tokunaga 2002; Tokunaga et al. 2002).

The observations were performed on three nights: 2006 November 8 UT, 2007 November 23 UT, and 2008 January 14 UT. Only on 2007 November 23 UT, the observing conditions were photometric. On 2006 November 8 UT, it was highly humid ($\sim 45\text{--}75\%$), while cirrus was sometimes seen on 2008 January 14 UT. Because the detector output linearity is not guaranteed for counts over $\sim 20,000$ ADU, we obtained short-exposure images in addition to long-exposure images for more sensitive detection. The exposure times for the long-exposure images are 120, 15, and 30 s for the J , H , and K_S bands, respectively, whereas the exposure time for short-exposure images is 13 s for all bands. The total integration times for the long-exposure images are 720, 420, and 960 s for the J , H , and K_S bands, respectively, whereas the total integration time for the short-exposure images is 52 s for all bands. The center of the images for S208 is set at $\alpha_{2000} = 04^{\text{h}}19^{\text{m}}45^{\text{s}}$, $\delta_{2000} = +53^{\circ}05'41''$, which covers the whole H II region described in Section 2.2 (see the white box in Figure 1 for the MOIRCS field). For background subtraction, we also obtained images of the sky, which is just to the north of the images for S208 by 5.5 arcmin, to avoid the nebulousity of S208. We summarize the details of the observation in Tab. 2.

3.2. Data Reduction and Photometry

All data in each band were reduced using IRAF⁹ with standard procedures, including flat fielding, bad-pixel correction, median-sky subtraction, image shifts with dithering offsets, and image combination. We used sky flats made from the archived MOIRCS data

in SMOKA¹⁰. We selected the data of the closest run. In addition to the above standard procedures, distortion correction was applied before image combination using the “MCSRED”¹¹ reduction package for the MOIRCS imaging data. We constructed a pseudocolor image of S207 by combining the long-exposure images for J (1.26 μm , blue), H (1.64 μm , green), and K_S (2.15 μm , red) bands (Figure 3).

JHK_S photometry was performed using the IRAF apphot package for stars in the north-east half-frame of the image for S208 (“S208 frame,” hereafter), where a star-forming cluster was detected (Figure 3; see Section 4.1). As photometric standards, 2MASS stars in these fields were used after converting the 2MASS magnitudes to the MKO magnitudes using the color transformations in Leggett et al. (2006).

Only 2MASS stars with good 2MASS photometric quality and with colors of $J - H \leq 0.5$, $H - K_S \leq 0.5$, and $J - K_S \leq 1.0$ were used to avoid the color term effect. Because the cluster is very crowded, we used an aperture diameter of $0''.7$ for cluster members to avoid contamination of adjacent stars. In the IRAF apphot package, only pixel-to-pixel standard deviation in the background sky region for each source is considered for the magnitude errors. In addition, we consider the flux uncertainty in the $0''.7$ aperture that is estimated for each frame from the standard deviation of the flux in about 3000 independent apertures in the blank area in the frame. As a result, the limiting magnitudes (10σ) of long-exposure images are $J = 19.8 \text{ mag}$, $H = 18.5 \text{ mag}$, and $K_S = 18.0 \text{ mag}$. Because the detection completeness of stars with $<10\sigma$ detection is less than one, whereas that of the brighter stars is almost one (see Yasui et al. 2008b and Minowa et al. 2005), we used only stars with all JHK_S magnitudes brighter than the limiting magnitudes (10σ) in the following.

4. A YOUNG EMBEDDED CLUSTER IN S208

4.1. Identification of a Young Cluster in S208

In the pseudocolor image of the observed field with MOIRCS (Figure 3), we detected a star cluster in the central region of S208 from the enhancement of stellar density compared to that of the surrounding area, which is reported in Bica et al. (2003). In addition, we found a small stellar association (hereafter, S208 association) located ~ 1.5 arcmin toward the southwest of the center of S208. We identified the position of the association by eye and show it with a yellow dashed circle. Both the cluster and the association are located near the region where the *WISE* band 3 (12 μm) emission is very strong (Figure 1); this combination is often seen in clusters (see Koenig et al. 2012). Because the cluster is only seen in the northwest part of the image, and because an engineering detector was used for the other half of the observation of long-exposure images¹², we used stars only in the northwest half-frame (the S208 frame) in the following discussion of this section. First, we defined the

⁹ IRAF is distributed by the National Optical Astronomy Observatories, which are operated by the Association of Universities for Research in Astronomy, Inc., under cooperative agreement with the National Science Foundation.

¹⁰ SMOKA is the Subaru–Mitaka–Okayama–Kiso Archive System operated by the Astronomy Data Center, National Astronomical Observatory of Japan.

¹¹ http://www.naoj.org/staff/ichi/MCSRED/mcsred_e.html

¹² http://www.subarutelescope.org/Observing/Instruments/MOIRCS/inst_detector.html

cluster region. We set many circles with 50 pixel ($\sim 6''$) radius in the S208 frame with 1 pixel step and counted the numbers of stars included in all circles (2 ± 2 stars on average). From these circles, we picked a circle that contains the maximum number of stars (approximately 30) to define the center of the cluster with an accuracy of $\sim 5''$: $\alpha_{2000} = 04^{\text{h}}19^{\text{m}}32.7^{\text{s}}$, $\delta_{2000} = +52^{\circ}58'34.6''$. Figure 4 shows the radial variation of the projected stellar density using stars with K_S magnitudes of ≤ 18.0 mag, corresponding to the 10σ detection limit. The horizontal solid line indicates the density of the region located by more than 500 pixel from the center of the S208 frame. We defined the cluster region with a circle having a radius of 300 pixel ($34''$), where the stellar density is more than that of the entire sky frame by 3σ . This is consistent with the cluster size estimated in Bica et al. (2003) for the 2MASS data (both major and minor angular dimensions of $1'.2$). The defined cluster region is shown as the yellow circle in Figure 3. The cluster radius corresponds to 1.6 pc and 0.7 pc with distances of $D = 9$ kpc and $D = 4$ kpc, respectively. We also defined a control field in the S208 frame that is the area located by more than 500 pixels from the center of the cluster region.

4.2. Color-Magnitude Diagram

We constructed the $J-K_S$ versus K_S color-magnitude diagrams of detected point sources in the S208 frame (Figure 5). The dwarf star tracks in spectral types of O9 to M6 (corresponding mass of $\sim 0.1-20 M_{\odot}$) by Bessell & Brett (1988) are shown as black lines, whereas the isochrone models for the age of 1 Myr are shown as blue lines. The isochrone models are by Lejeune & Schaerer (2001) for the mass of $7 < M/M_{\odot} \leq 40$, by Siess et al. (2000) for the mass of $3 < M/M_{\odot} \leq 7$, and by D'Antona & Mazzitelli (1997, 1998) for the mass of $0.017 \leq M/M_{\odot} \leq 3$. Distances of 9 kpc and 4 kpc are assumed. The arrow shows the reddening vector of $A_V = 5$ mag. In the color-magnitude diagram, the extinction A_V of each star was estimated from the distance between its location and the isochrone models along the reddening vector. For convenience, the isochrone model is approximated as a straight line, shown in solid gray. We then constructed the distributions of the extinctions of stars in the cluster region (black) and in the control field (gray) in Figure 6. The distribution for the control field is normalized to match the total area of the cluster regions. The resultant distribution for the control field shows a peak at $A_V \sim 2$ mag, whereas that for the cluster region shows a peak at the much larger extinction of $A_V \sim 6-8$ mag. Because the differences between the two distributions are significant, cluster members can be distinguished from contamination stars in the cluster region based on the values of A_V , as in the case with the Cloud 2 clusters (Yasui et al. 2009). We found that stars with $A_V \geq 4.0$ mag are concentrated on the cluster region, while stars with $A_V < 4.0$ mag are widely distributed over the observed field. The following criteria are applied to identify members of the S208 cluster: (1) they are distributed in the cluster regions, and (2) have large A_V excess compared with normal field stars (extinction of $A_V \geq 4$ mag). Actually, on the color-magnitude diagram, the cluster members are located in the region clearly separated from the region for normal field stars. In Figure 5, the identified cluster members are shown by red circles

while all other sources in the S208 frame are shown by black dots. As a result, 89 sources (N_{cl}) are identified as S208 cluster members. The average A_V value of the cluster members is estimated at $A_V = 10.1 \pm 3.9$ mag.

Considering the relatively large R_G of the S208 clusters ($R_G \geq 12$ kpc), the contamination of background stars can be negligible and most of the field objects are foreground stars (some are background galaxies). To quantify the contamination, we compared the A_V distributions of all the sources in the cluster regions and the field objects in the control field (Figure 6). Because the number of field objects decreases significantly at $A_V \geq 4$ mag, most cluster members can be distinguished from the field objects as red sources with $A_V \geq 4$ mag. The contamination by the foreground stars is estimated at $\sim 2\%$ by counting the normalized number of field objects in the tail of the distribution at $A_V \geq 4$ mag and dividing it by the total number of sources in the cluster regions. In contrast, there must be some cluster members at $A_V < 4$ mag that missed our identification. Using the normalized number of field objects with $A_V \geq 4$ mag (N'_{fi}), the number of stars in the cluster region with $A_V \geq 4$ mag (N'_{cl}), and the number of identified cluster members (N_{cl}), the contamination is estimated to be $\sim 6\%$ from $(N'_{\text{cl}} - N'_{\text{fi}})/(N_{\text{cl}} + (N'_{\text{cl}} - N'_{\text{fi}}))$.

We placed the short horizontal lines on the isochrone models shown in the same colors as the isochrone tracks, which show the positions of 0.1, 1, 3, and $10 M_{\odot}$. Assuming the average A_V of 10.1 mag, the K -band limiting magnitude of 18.0 mag (10σ) for the age of 1 Myr corresponds to masses of $0.9 M_{\odot}$ and $0.2 M_{\odot}$ in the cases of photometric distance $D = 9$ kpc and kinematic distance $D = 4$ kpc, respectively. In any case, the mass detection limit is sufficiently low, down to the substellar mass, which enables us to estimate the age using KLF (Section 5.1) and to derive the disk fraction with the same criteria as in the solar neighborhood (Section 5.3). Because the most likely age and distance of S208 are estimated at ~ 0.5 Myr and ~ 4 kpc in Section 5.1, respectively, the mass detection limit is then $\sim 0.2 M_{\odot}$.

4.3. Color-Color Diagram

In Figure 7, we show the $J-H$ versus $H-K_S$ color-color diagram for stars in the S208 frame. The cluster members are shown as red circles, while all other sources are shown as black dots. The dwarf star track in the late B to M6 spectral types in the MKO system by Yasui et al. (2008b) is the solid curve. The classical T Tauri star (CTTS) locus, originally derived by Meyer et al. (1997) in the CIT system, is shown as a gray line in the MKO system (Yasui et al. 2008b). The arrow shows the reddening vector of $A_V = 5$ mag. Stars with circumstellar dust disks are known to show a large $H-K$ color excess (e.g., Lada & Adams 1992).

The intrinsic $(H-K)$ colors ($(H-K)_0$) of each star were estimated by dereddening along the reddening vector to the young star locus in the color-color diagram (see Figure 7). For convenience, the young star locus was approximated by the extension of the CTTS locus, and only stars that are above the CTTS locus were used. We constructed intrinsic $H-K$ color distributions for the S208 cluster members and for those in the control field in Figure 8. The distribution for the control field is normalized to match the total area of the cluster regions. The dis-

tribution of the cluster members seems to have a larger number of red stars with $(H - K)_0 > 0.2$ mag compared to those in the control field. The average $(H - K)_0$ value for cluster members is estimated at 0.35 mag, whereas that in the control field is estimated at 0.23 mag. The difference in the average $(H - K)_0$ between the stars in the cluster region and in the field stars (0.12 mag) can be attributed to thermal emission from the circumstellar disks of the cluster members. Assuming that disk emissions appear in the K band but not in the H band, the disk color excess of the S208 cluster members in the K band, ΔK_{disk} , is equal to 0.12 mag.

4.4. K -band Luminosity Function (KLF)

We constructed the KLF for the S208 cluster members (black line in Figure 9). The number counts of the KLF generally increase in the fainter magnitude bins. However, the number counts become flat in the $K = 15.5$ – 16.5 mag bin and they then decrease in the $K = 17.5$ mag bin, which generally corresponds to the peak of IMF. Considering the 10σ detection magnitude of $K = 18.0$ mag for the S208 frame, the completeness should be ~ 1 in all the magnitude bins (Section 3.2; see also Yasui et al. 2008b and Minowa et al. 2005). Therefore, even considering the detection completeness, the S208 KLF would have a peak at the $K = 15.5$ – 16.5 mag bin.

It should be noted that the large A_V dispersion of the S208 cluster, $A_V \sim 4$ – 25 mag, can make it difficult to detect faint cluster members. This may be the cause for the decrease of the KLF in fainter magnitude bins. For comparison, we also constructed KLFs for stars with limited A_V values in Figure 9, $A_V = 5$ – 15 mag and $A_V = 6.2$ – 13.0 mag (from the A_V distribution of the cluster members, 10.1 ± 3.9 mag), which are shown by the solid and dashed gray lines, respectively. For clarity, the KLFs are shifted vertically by $+0.1$ mag and $+0.2$ mag for the KLFs of stars with $A_V = 5$ – 15 mag and $A_V = 6.2$ – 13.0 mag, respectively. As a result, the discrepancy between all three KLFs are found to be within the uncertainty range, suggesting that the selection of stars with different limited A_V values causes a negligible influence on the obtained KLF. Therefore, we used the original KLF (KLF from all S208 cluster members) in the following discussion.

5. DISCUSSION

5.1. Age and Distance of S208

The KLFs of different ages are known to have different peak magnitudes and slopes, fainter peak magnitudes and less steep slopes with increasing age (Muench et al. 2000). By comparing observed and model KLFs, the age of the young clusters can be roughly estimated with an uncertainty of ± 1 Myr (Yasui et al. 2006, 2008b). We constructed model KLFs in the same way as in our previous work (see Section 4 in Yasui et al. 2006) with the assumed distance of the cluster that underlies typical IMFs and mass–luminosity relations. We used the Trapezium IMF (Muench et al. 2002), which is considered to be the most reliable IMF for young clusters (e.g., Lada & Lada 2003), as discussed in Yasui et al. (2008b). We used isochrone models in Section 4.2: models by Lejeune & Schaerer (2001) for the high-mass

range ($7 < M/M_\odot \leq 40$), by Siess et al. (2000) for the intermediate-mass range ($3 < M/M_\odot \leq 7$), and by D’Antona & Mazzitelli (1997, 1998) for the low-mass range ($0.017 \leq M/M_\odot \leq 3$). We constructed model KLFs with ages of 0.1, 0.5, 1, 2, and 3 Myr assuming the kinematic distance ($D = 9$ kpc; Figure 10, left) and the photometric distance ($D = 4$ kpc; Figure 10, right). We also considered the A_V and ΔK_{excess} estimated in Sections 4.2 and 4.3.

We compared the observed KLF (black lines in Figure 10) and model KLFs, constructed in the same way as in Yasui et al. (2006, 2008b; colored lines in Figure 10), for the two distances. The model KLFs were normalized so that the total number of stars in the magnitude range $K = 12$ – 18 mag is the same as that for the observed KLF. In the case of $D = 9$ kpc (Figure 10, left), the peak magnitude of the observed KLF ($K = 15.5$ – 16.5 mag) is found to be much brighter than those of the model KLFs for any ages of more than 0.1 Myr ($K \geq 18.5$ mag). The peak magnitude of the observed KLF corresponds to $\sim 3 M_\odot$ for the model KLF with the age of 0.1 Myr. The corresponding mass becomes even larger for older ages, which is obviously implausible for the peak mass of the underlying IMF. Therefore, the quoted photometric distance, $D = 9$ kpc, does not seem to be correct. On the other hand, in the case of $D = 4$ kpc (Figure 10, right), the model KLFs with ages of 0.1–0.5 Myr appear to fit the observed KLF for both the peak and slope of the KLF. However, it is difficult to estimate the age of the cluster with an accuracy of 0.1 Myr because isochrone models for ages of less than 1 Myr are thought to be uncertain (e.g., Baraffe et al. 2002). Therefore, the age of ~ 0.5 Myr and the distance of $D = 4$ kpc are most likely parameters for the S208 cluster. The suggested distance of the S208 cluster is consistent with the kinematic distance and with S208 being located in the outer arm, as described in Section 2.1. This is also the case for S207 (see Yasui et al. 2016), except that S207 is slightly older (~ 2 – 3 Myr). Therefore, both H II regions appear to make a combination in the outer arm. We will discuss the star formation for those two H II regions in the outer arm in Section 6.

5.2. Implication for IMF

CO emission was detected in S208 by Blitz et al. (1982) and Wouterloot & Brand (1989) as described in Section 2.1. Although the CO emission by Wouterloot & Brand (1989) does not cover the cluster region, that by Blitz et al. (1982) totally covers the region¹³. Based on the physical parameters estimated by Blitz et al. (1982), $T_A^* = 13$ K and $\Delta V = 9.8$ km s^{−1}, the H₂ column density¹⁴ is estimated to be ~ 4 – 5×10^{22} cm^{−2}, which corresponds to $A_V = 50$ mag. Considering that

¹³ The central position of the CO emission in Wouterloot & Brand (1989) is more than $100''$ apart from the IRAS positions (plus symbol in Figure 1) with the beam size of their observation ($21''$), while that by Blitz et al. (1982) is about $30''$ off the center of the S208 cluster region with the beam size of $\sim 2''$ in their observation.

¹⁴ The telescopes at the Bell Telescope Laboratories (BTL) and the Millimeter Wave Observatory (MWO) were used for the S208 observation in Blitz et al. (1982). The column density is estimated considering a main beam efficiency of 89% for BTL (Bally et al. 1987) and $\sim 80\%$ for MWO (Magnani et al. 1985).

the molecular gas disperses on a timescale of ~ 3 Myr (Hartmann et al. 2001), the age of the S208 cluster is at least $\lesssim 3$ Myr. The high column density suggests a quite young age. However, for a more precise distribution of the CO molecular cloud relative to the cluster, CO mapping with high sensitivity will be necessary in the future.

In Section 4.3, the average extinction of stars in the S208 cluster is estimated at $\langle A_V \rangle \sim 10$ mag with a peak of $A_V = 6$ –8 mag. Considering $A_V \sim 3$ mag for the foreground extinction in the direction of S208, which was estimated from a three-dimensional extinction map of the Galactic plane (Sale et al. 2014), the average intrinsic extinction of the S208 cluster is estimated at $\langle A_V \rangle \sim 7$ mag. Generally, the average extinction is higher for younger clusters: $\langle A_V \rangle \sim 11$ mag for NGC 2024 (~ 0.5 Myr old) by Meyer et al. (2008; see also Haisch et al. 2000), $\langle A_V \rangle = 9$ mag for Orion Trapezium (~ 1 Myr old) by Muench et al. (2002), $\langle A_V \rangle = 3.5$ mag for IC 348 (2.5 Myr old) by Herbst (2008), and $\langle A_V \rangle = 0.5$ mag for NGC 2264 (3 Myr old) by Rebull et al. (2002). The S208 cluster shows the high extinction that is similar to NGC 2024 and Trapezium, suggesting that the age of the S208 cluster is quite young, ~ 0.5 –1 Myr. Because extinctions can be estimated lower considering the low metallicity of S208 (see e.g., Garn & Best 2010), the actual gas mass may be larger, implying that the S208 cluster is even younger.

In the KLF fitting (Section 5.1), a typical IMF is assumed for estimating the age of the S208 cluster. We found that the estimated age (~ 0.5 Myr) is consistent with the above roughly estimated age based on independent information. This suggests that the IMF of the S208 cluster, which is located in very low-metallicity environments, can be approximated by the typical IMFs of the solar neighborhood (~ 0 dex) for the mass range of $\geq 0.2 M_\odot$. Because the KLF slope on the bright side is very sensitive to the higher-mass slope of the IMF (Yasui et al. 2006, 2008a), the good fit of the observed KLF down to the peak at $m_K \sim 16$ mag suggests that the higher-mass slope of the IMF is not significantly different from typical IMFs. The characteristic mass (M_c), which is the mass of the IMF peak corresponding to the peak of the KLF, is estimated at $\sim 0.6 M_\odot$ for the age of 0.5 Myr. This is identical to the characteristic mass of the IMF in the solar neighborhood, $M_c \sim 0.3 M_\odot$ ($\log M_c/M_\odot \sim -0.5 \pm 0.5$; Elmegreen et al. 2008). Similarly, the universal IMF has also been suggested in our previous studies of other young clusters in low-metallicity environments, Cloud 2-N, -S clusters (Yasui et al. 2006, 2008b), and S207 (Yasui et al. 2016).

5.3. Disk Fraction

The ratio of stars with protoplanetary disks in young clusters, the disk fraction, is one of the most fundamental parameters characterizing disk formation and evolution, and ultimately planet formation (Haisch et al. 2001; Lada & Lada 2003). On the *JHK* color-color diagram, stars without circumstellar disks are seen as main-sequence stars reddened with extinction, whereas stars with circumstellar disks are seen in “the disk-excess region,” which is the orange highlighted region to the right of the dot-dashed line in Figure 7 because of thermal emissions from a hot dust disk with a temperature of ~ 1500 K. The dot-dashed line intersecting the dwarf star

curve at maximum $H - K_S$ values (M6 point on the curve) and is parallel to the reddening vector is the border between stars with and without circumstellar disks (see details in Yasui et al. 2009). The disk fraction for identified cluster members with more than 10σ detection for all *JHK_S* bands is estimated at $27 \pm 6\%$ (24/89) from Figure 7.

In Figure 11, we show the fraction of stars (f_{stars}) per each intrinsic $(H - K)$ color bin $(H - K)_0$ for the S208 cluster (red), which is shown as the black line in Figure 8, and those for other young clusters in low-metallicity environments, S207 (black solid line), Cloud 2-N (black dashed line), and Cloud 2-S (black dotted line) with estimated disk fractions of 4%, 9%, and 27%, respectively (Yasui et al. 2009). The vertical dashed line shows the borderline for estimating the disk fraction in the MKO system.¹⁵ The distribution becomes bluer and sharper with lower disk fractions for nearby young clusters (see the bottom panel of Figure 7 in Yasui et al. 2009), which is also the case for clusters in low-metallicity environments (Yasui et al. 2009). The peak $(H - K)_0$ of the S208 cluster is relatively red, $(H - K)_0 \sim 0.3$ mag, while the distribution is relatively broad with the maximum a $(H - K)_0$ of ~ 2 mag. The distribution of the S208 cluster resembles that of the Cloud 2-S cluster with a disk fraction of $\sim 25\%$ rather than those of the S207 cluster and the Cloud 2-N cluster with a disk fraction of $< 10\%$. The distribution of the S208 cluster is consistent with the estimated disk fraction, $27 \pm 6\%$.

NIR disk fractions are known to have high values ($\sim 60\%$) for very young clusters but decrease with increasing age, and then reach ~ 5 –10% on a timescale of ~ 10 Myr (Lada 1999; Hillenbrand 2005; Yasui et al. 2010; see the red line in the left panel of Fig 5 in Yasui et al. 2014). Although NIR disk fractions are generally slightly lower than MIR disk fractions, which are based on ground *L*-band observations and space MIR observations, the characteristics are quite similar. As suggested in Yasui et al. (2010), the derived disk fraction for the S208 cluster ($27 \pm 6\%$) is lower than that for clusters in the solar neighborhood with ages similar to the S208 cluster’s age ($\sim 60\%$ for < 1 Myr). The lower disk fraction in low-metallicity environments suggests that the disk lifetime in low-metallicity environments is quite short, as discussed in Yasui et al. (2009).

It should be noted that only the S208 cluster has very red stars with $(H - K)_0 \geq 1.5$ mag in Figure 11. This may be because the cluster is the youngest among those in Figure 11: the estimated age of the S208 cluster is ~ 0.5 Myr (Section 5.1), while those of the Cloud 2-N, Cloud 2-S, and S207 clusters are 0.5–1 Myr, 0.5–1 Myr, and 2–3 Myr, respectively (see Yasui et al. 2016 and references therein). Very young YSOs that are surrounded by thick circumstellar envelopes of falling material, called Class I sources, are known to show very red NIR colors (Kenyon & Hartmann 1995). Although the classification of sources between Class I and Class II (YSOs surrounded by optically thick circumstellar disks) cannot be perfectly distinguished using the *JHK* color-color diagram, many of the Class I sources in NGC 2024 are

¹⁵ Although $(H - K)_0 = 0.43$ mag was shown for the borderline in the MKO system in Yasui et al. (2009), we found that the correct borderline is $(H - K)_0 = 0.52$ mag.

located in the disk-excess region and have large $J - K$ colors (equal to the sum of $J - H$ (y-axis) and $H - K$ (x-axis) colors) of larger than ~ 3 (see left panel of Figure 8 in Haisch et al. 2000). The same trend is seen in the Taurus star-forming region.¹⁶ The S208 cluster has four objects with such colors. Our results suggest that YSOs in low-metallicity environments are initially surrounded by thick circumstellar envelopes, as is the case for the solar neighborhood, but the circumstellar material as well as the disk disperse very quickly.

6. STAR FORMATION IN THE OUTER ARM

Figure 12 (left) shows a *WISE* MIR pseudocolor image around S207 and S208 with a field of view of $30 \text{ arcmin} \times 30 \text{ arcmin}$ centered at $(l, b) = (151.24^\circ, +2.05^\circ)$ in Galactic coordinates. S207 is located in the upper right in the figure, while S208 is located in the lower left, $\sim 10 \text{ arcmin}$ southward of S207. Since the identical distances of S207 and S208, $\sim 4 \text{ kpc}$, are supported both from the kinematic distance and from the KLF fitting (Section 5.1 in Yasui et al. 2016 for S207, and Section 5.1 for S208), the actual separation is suggested to be very small, 12 pc . Based on the distance, their Galactrocentric distances are estimated at $R_G \simeq 12 \text{ kpc}$, suggesting that both clusters are located in the outer arm (Figure 2). The fact that the kinematic distance is consistent with the photometric (KLF) distance may support the suggestion that sources in the outer arm are in nearly circular Galactic orbits (e.g., Hachisuka et al. 2015).

Because the estimated metallicities of both clusters are also almost identical, -0.8 dex , the star-formation activities in the two clusters are suggested to originate in a similar environment, except that they are at different evolutionary stages: S207 is suggested to be at the end of the embedded cluster phase ($\sim 2\text{--}3 \text{ Myr}$), while S208 is suggested to be in a very young phase ($\sim 0.5 \text{ Myr}$) from the KLF fitting. This is also suggested from the NIR pseudocolor images, the bluer colors of the S207 cluster (Figure 1, bottom in Yasui et al. 2016), and the redder colors of the S208 cluster (see Figure 3). The differences in the following two star-forming properties of the star formation support the difference in the cluster ages. (i) Cluster size. The cluster size is suggested to be larger with increasing ages due to proper motions of individual stars (Stahler & Palla 2005). This is the case for the S207 and S208 clusters: the sizes are about 1.3 pc and 0.7 pc in radius, respectively. These radii are consistent with those in the cluster samples of Pfalzner & Eckart (2009), in which many of them are nearby clusters (see Figure 2b in Pfalzner & Eckart 2009). (ii) Size of an H II region. Size of an H II region is known to become larger with an increasing age (Dyson & Williams 1980). This is the case for S207 and S208: the radius of 3 pc for S207 and that of 1.2 pc for S208 from the 1.4 GHz radio continuum. An $\text{H}\alpha$ image (Figure 12, right) from the IPHAS survey (Drew et al. 2005) around S207 and S208 also shows the clear difference in size of the two H II regions. Dyson & Williams (1980) inferred the age of the H II region with the assumption of a uniform pressure within the ionized region. According to this model, the age is

estimated to be 0.2 Myr for S207 and 0.1 Myr for S208 assuming an original ambient density of $n = 10^3 \text{ cm}^{-3}$ and a flux of ionizing photons for the H II regions (N_{Ly}) of $1.25 \times 10^{48} \text{ s}^{-1}$ emitted from a B0V star (Vacca et al. 1996; Schaerer & de Koter 1997). Although this age estimate is crude because the assumption of evolution in a strictly uniform medium is unrealistic (Deharveng et al. 2006), the trends in the size of the H II region for S207 and S208 should reflect the age sequence.

Figure 13 shows a *WISE* MIR pseudocolor image around S207 and S208 with a wide field of view ($2^\circ \times 2^\circ$)¹⁷ centered at $(l, b) = (151.19^\circ, +2.13^\circ)$ in the Galactic coordinates. Black circles show the positions and sizes of the S207 cluster, the S208 cluster, and the S208 association (see Section 4.1). The cyan crosses show the locations of IRAS point sources, while the black crosses show some specific features, 2MASX J04183258+5326027 and Waterloo 1 (Wat 1), in the SIMBAD online database. 2MASX J04183258+5326027 is an H_2O maser source, which is a signature of massive star formation, while Wat 1 is a star cluster (Moffat et al. 1979). In the figure, a bubble-like structure (a white dashed ellipse) with $\sim 22 \times 27 \text{ arcmin}$ radius is seen, where S207 appears to be located around the edge. The corresponding size of the bubble is $\sim 26 \times 33 \text{ pc}$ at the distance of 4 kpc , which is a relatively large structure compared to those in the *WISE* MIR survey of massive star-forming regions by Koenig et al. (2012), $3\text{--}24 \text{ pc}$, although it is smaller than superbubbles with radius of $\sim 100\text{--}1000 \text{ pc}$ (e.g., Sato et al. 2008). Bubbles are thought to be one of the major triggers of star formation (e.g., Deharveng et al. 2010, Koenig et al. 2012). Possible star-forming regions are located around the bubble: many IRAS point sources are located inside and around the edge bubble, while 2MASX J04183258+5326027 appears to be located around the edge of the bubble. They suggest that the bubble triggers star formation in S207 and the above regions. The bubble feature is not significant in the higher latitudes, while the feature is prominent in the lower latitudes. Also, many possible star-forming regions are distributed in the lower latitude on the line extending to S207, S208 (the S208 cluster and the S208 association), Wat 1, and many IRAS point sources. Because the radial velocity of Wat 1 is comparable to those of S207 and S208, Wat 1 is suggested to actually be located at the identical distance (Foster & Brunt 2015). The positional relationship between S207, S208, and possible star-forming regions suggests that the bubble also triggers star formation in the lower latitudes and that sequential star formation is occurring. This is consistent with the age difference between the S207 cluster and the S208 cluster, i.e., younger in the S207 and older in S208. Because no massive stars¹⁸, H II regions, or supernova remnants are identified around the center of the bubble in the SIMBAD online database, we cannot tell how this bubble was made at this stage.

There are two major paradigms for triggered star for-

¹⁷ We used Image Co-addition with Optional Resolution Enhancement software (Masci & Fowler 2009) for producing customized images with *WISE* single-exposure images.

¹⁸ There is only one O-type star in the field of view from the SIMBAD online data base, GSC 03719-00546, which is located around the center of S207 and is a probable dominantly exciting source of it.

¹⁶ We checked the colors of the Class I sources in the Taurus with NIR photometry data by Kenyon & Hartmann (1995) and information of classifications by Kenyon et al. (1998).

mation: “collect and collapse” (Elmegreen & Lada 1977) and “radiation-driven implosion” (Bertoldi 1989). There are no significant shell-like structures with neutral gas, which are characteristics of the collect and collapse scenario (Deharveng et al. 2010), around S207 and S208 in the H I data (see the bottom left panel of Figure 3 in Foster & Brunt 2015). The pillar structures, which are often seen in locations where star formation may be triggered via radiatively driven implosion (e.g., Sugitani & Ogura 1994), are seen around the bubble and in the lower Galactic latitude of Wat 1. They suggest that the star formation in this area is likely due to radiation-driven implosion rather than the collect and collapse scenario. However, further studies in larger scales by multiwavelength observations (e.g., Kobayashi et al. 2008) are necessary in the future for concluding the star formation triggers for the twin H II regions, S207 and S208.

This work was supported by JSPS KAKENHI Grant Number 26800094 and MEXT KAKENHI Grant Number 23103004. We thank the Subaru support staff, in particular, the MOIRCS support astronomer Ichi Tanaka. We also thank Chihiro Tokoku for helpful discussions on the observation.

REFERENCES

- Asplund, M., Grevesse, N., Sauval, A. J., & Scott, P. 2009, *ARA&A*, 47, 481
- Bally, J., Stark, A. A., Wilson, R. W., & Henkel, C. 1987, *ApJS*, 65, 13
- Baraffe, I., Chabrier, G., Allard, F., & Hauschildt, P. H. 2002, *A&A*, 382, 563
- Beichman, C. A., Neugebauer, G., Habing, H. J., Clegg, P. E., & Chester, T. J. 1988, *Infrared Astronomical Satellite (IRAS) Catalogs and Atlases*, Vol. 1, 1
- Bertoldi, F. 1989, *ApJ*, 346, 735
- Bessell, M. S., & Brett, J. M. 1988, *PASP*, 100, 1134
- Bica, E., Dutra, C. M., Soares, J., & Barbuy, B. 2003, *A&A*, 404, 223
- Blitz, L., Fich, M., & Stark, A. A. 1982, *ApJS*, 49, 183
- Bono, G., Matsunaga, N., Inno, L., Lagioia, E. P., & Genovali, K. 2013, *Cosmic Rays in Star-Forming Environments*, 34, 115
- Brandl, B., Sams, B. J., Bertoldi, F., et al. 1996, *ApJ*, 466, 254
- Caplan, J., Deharveng, L., Peña, M., Costero, R., & Blondel, C. 2000, *MNRAS*, 311, 317
- Chini, R., & Wink, J. E. 1984, *A&A*, 139, L5
- Condon, J. J., Cotton, W. D., Greisen, E. W., et al. 1998, *AJ*, 115, 1693
- Crampton, D., Georgelin, Y. M., & Georgelin, Y. P. 1978, *A&A*, 66, 1
- D’Antona, F., & Mazzitelli, I. 1997, *Memorie della Societa Astronomica Italiana*, 68, 807
- D’Antona, F., & Mazzitelli, I. 1998, in *ASP Conf. Ser. 134: Brown Dwarfs and Extrasolar Planets*, ed. R. Rebolo, E. L. Martin, & M. R. Z. Osorio (San Francisco, CA: ASP), 442
- Deharveng, L., Lefloch, B., Massi, F., et al. 2006, *A&A*, 458, 191
- Deharveng, L., Peña, M., Caplan, J., & Costero, R. 2000, *MNRAS*, 311, 329
- Deharveng, L., Schuller, F., Anderson, L. D., et al. 2010, *A&A*, 523, A6
- Drew, J. E., Greimel, R., Irwin, M. J., et al. 2005, *MNRAS*, 362, 753
- Dyson, J. E., & Williams, D. A. 1980, (New York: Halsted Press), 204
- Elmegreen, B. G., & Lada, C. J. 1977, *ApJ*, 214, 725
- Elmegreen, B. G., Klessen, R. S., & Wilson, C. D. 2008, *ApJ*, 681, 365
- Fich, M. 1993, *ApJS*, 86, 475
- Foster, T., & Brunt, C. M. 2015, *AJ*, 150, 147
- Garn, T., & Best, P. N. 2010, *MNRAS*, 409, 421
- Hachisuka, K., Choi, Y. K., Reid, M. J., et al. 2015, *ApJ*, 800, 2
- Haisch, K. E., Jr., Lada, E. A., & Lada, C. J. 2000, *AJ*, 120, 1396
- Haisch, K. E., Jr., Lada, E. A., & Lada, C. J. 2001, *ApJ*, 553, L153
- Hartmann, L., Ballesteros-Paredes, J., & Bergin, E. A. 2001, *ApJ*, 562, 852
- Herbst, W. 2008, in *Handbook of Star Forming Regions: The Northern Sky*, Vol. 1, ed. B. Reipurth (San Francisco, CA: ASP), 372
- Hillenbrand, L. A. 2005, *ArXiv Astrophysics e-prints*, arXiv:astro-ph/0511083
- Ichikawa, T., Suzuki, R., Tokoku, C., et al. 2006, *Proc. SPIE*, 6269, 626916
- Kenyon, S. J., Brown, D. I., Tout, C. A., & Berlind, P. 1998, *AJ*, 115, 2491
- Kenyon, S. J., & Hartmann, L. 1995, *ApJS*, 101, 117
- Kobayashi, N., Yasui, C., Tokunaga, A. T., & Saito, M. 2008, *ApJ*, 683, 178
- Koenig, X. P., Leisawitz, D. T., Benford, D. J., et al. 2012, *ApJ*, 744, 130
- Korotin, S. A., Andrievsky, S. M., Luck, R. E., et al. 2014, *MNRAS*, 444, 3301
- Lada, C. J., & Adams, F. C. 1992, *ApJ*, 393, 278
- Lada, C. J., & Lada, E. A. 2003, *ARA&A*, 41, 57
- Lada, E. A. 1999, in *The Origin of Stars and Planetary Systems*, ed. C. J. Lada & N. D. Kylafis (Dordrecht: Kluwer), 441
- Lahulla, J. F. 1985, *A&AS*, 61, 537
- Leggett, S. K., Currie, M. J., Varricatt, W. P., et al. 2006, *MNRAS*, 373, 781
- Lejeune, T., & Schaerer, D. 2001, *A&A*, 366, 538
- Luck, R. E., Kovtyukh, V. V., & Andrievsky, S. M. 2006, *AJ*, 132, 902
- Magnani, L., Blitz, L., & Mundy, L. 1985, *ApJ*, 295, 402
- Masci, F. J., & Fowler, J. W. 2009, in *ASP Conf. Ser. 411, Astronomical Data Analysis Software and Systems XVIII*, ed. D. A. Bohlender, D. Durand & P. Dowler (San Francisco, CA: ASP), 67
- Meyer, M. R., Calvet, N., & Hillenbrand, L. A. 1997, *AJ*, 114, 288
- Meyer, M. R., Flaherty, K., Levine, J. L., et al. 2008, in *Handbook of Star Forming Regions*, Vol. I, ed. B. Reipurth (San Francisco, CA: ASP), 662
- Minowa, Y., Kobayashi, N., Yoshii, Y., et al. 2005, *ApJ*, 629, 29
- Moffat, A. F. J., Jackson, P. D., & Fitzgerald, M. P. 1979, *A&AS*, 38, 197
- Muench, A. A., Lada, E. A., & Lada, C. J. 2000, *ApJ*, 533, 358
- Muench, A. A., Lada, E. A., Lada, C. J., & Alves, J. 2002, *ApJ*, 573, 366
- Pfalzner, S., & Eckart, A. 2009, *A&A*, 508, L5
- Rebull, L. M., Makidon, R. B., Strom, S. E., et al. 2002, *AJ*, 123, 1528
- Rudolph, A. L., Fich, M., Bell, G. R., Norsen, T., Simpson, J. P., Haas, M. R., & Erickson, E. F. 2006, *ApJS*, 162, 346
- Russeil, D. 2003, *A&A*, 397, 133
- Sale, S. E., Drew, J. E., Barentsen, G., et al. 2014, *MNRAS*, 443, 2907
- Sato, M., Hirota, T., Honma, M., et al. 2008, *PASJ*, 60, 975
- Sharpless, S. 1953, *ApJ*, 118, 362
- Sharpless, S. 1959, *ApJS*, 4, 257
- Schaerer, D., & de Koter, A. 1997, *A&A*, 322, 598
- Siess, L., Dufour, E., & Forestini, M. 2000, *A&A*, 358, 593
- Simons, D. A., & Tokunaga, A. 2002, *PASP*, 114, 169
- Skrutskie, M. F., Cutri, R. M., Stiening, R., et al. 2006, *AJ*, 131, 1163
- Smartt, S. J., Venn, K. A., Dufton, P. L., et al. 2001, *A&A*, 367, 86
- Stahler, S. W., & Palla, F. (ed.) 2005, *The Formation of Stars* (New York: Wiley-VCH), 865
- Sugitani, K., & Ogura, K. 1994, *ApJS*, 92, 163
- Suzuki, R., Tokoku, C., Ichikawa, T., et al. 2008, *PASJ*, 60, 1347
- Tokunaga, A. T., Simons, D. A., & Vacca, W. D. 2002, *PASP*, 114, 180
- Vacca, W. D., Garmany, C. D., & Shull, J. M. 1996, *ApJ*, 460, 914

- Vallée, J. P. 2005, *AJ*, 130, 569
Wenger, M., Ochsenbein, F., Egret, D., et al. 2000, *A&AS*, 143, 9
Wright, E. L., Eisenhardt, P. R. M., Mainzer, A. K., et al. 2010, *AJ*, 140, 1868
Wouterloot, J. G. A., & Brand, J. 1989, *A&AS*, 80, 149
Yasui, C., Kobayashi, N., Tokunaga, A. T., & Saito, M. 2014, *MNRAS*, 442, 2543
Yasui, C., Kobayashi, N., Tokunaga, A. T., Saito, M., & Izumi, N. 2016, *AJ*, 151, 50
Yasui, C., Kobayashi, N., Tokunaga, A. T., Saito, M., & Tokoku, C. 2008a, in *ASP Conf. Ser.* 396, *Formation and Evolution of Galaxy Disks*, ed. J. G. Funes, S. J., & E. M. Corsini (San Francisco, CA: ASP), 225
Yasui, C., Kobayashi, N., Tokunaga, A. T., Saito, M., & Tokoku, C. 2009, *ApJ*, 705, 54
Yasui, C., Kobayashi, N., Tokunaga, A. T., Saito, M., & Tokoku, C. 2010, *ApJL*, 723, L113
Yasui, C., Kobayashi, N., Tokunaga, A. T., Terada, H., & Saito, M. 2006, *ApJ*, 649, 753
Yasui, C., Kobayashi, N., Tokunaga, A. T., Terada, H., & Saito, M. 2008b, *ApJ*, 674, 443
Yong, D., Carney, B. W., & Friel, E. D. 2012, *AJ*, 144, 95

Table 1
Properties of S208.

Name	Sh 2-208
Galactic longitude (deg)	151.2870 (1)
Galactic latitude (deg)	+1.9682 (1)
R.A. (J2000.0)	04 19 32.92 (1)
Decl. (J2000.0)	+52 58 41.6 (1)
Photometric heliocentric distance (kpc)	7.6 (2), 9.4 (3), 10.0 (4)
Adopted photometric heliocentric distance (kpc)	9
Photometric Galactocentric distance ^a (kpc)	$\simeq 16.5$
Kinematic heliocentric distance (kpc)	4.0 (5), 4.1 (6), 4.4 (7)
Adopted kinematic heliocentric distance (kpc)	4
Kinematic Galactocentric distance ^a (kpc)	$\simeq 12$
Oxygen abundance $12 + \log(\text{O}/\text{H})$	7.91 (6, 8)
Metallicity $[\text{O}/\text{H}]$ (dex) ^b	-0.8

Notes. References are shown in the parenthesis.

^aAssuming the solar Galactocentric distance $R_{\odot} = 8.0$ kpc.

^bAssuming the solar abundance of $12 + \log(\text{O}/\text{H}) = 8.73$ (Asplund et al. 2009).

References. (1) SIMBAD (Wenger et al. 2000), (2) Moffat et al. (1979), (3) Chini & Wink (1984), (4) Lahulla (1985), (5) Wouterloot & Brand (1989), (6) Caplan et al. (2000), (7) Foster & Brunt (2015), and (8) Rudolph et al. (2006).

Table 2
Summary of MOIRCS Observations.

Modes	Date	Band	t_{total} (1)	t (2)	Coadd (3)	N_{total} (4)	Seeing	Sky Condition (5)
<i>J</i> -long	2008 Jan 14	<i>J</i>	720 (480)	120	1	6 (4)	0''.6	C
<i>H</i> -long	2007 Nov 23	<i>H</i>	420 (315)	15	7	4 (3)	0''.9	P
<i>K_S</i> -long	2007 Nov 23	<i>K_S</i>	960 (720)	30	4	8 (6)	1''.0	P
<i>J</i> -short	2006 Nov 8	<i>J</i>	52 (39)	13	1	4 (3)	1''.2	H
<i>H</i> -short	2006 Nov 8	<i>H</i>	52 (39)	13	1	4 (3)	1''.2	H
<i>K_S</i> -short	2006 Nov 8	<i>K_S</i>	52 (39)	13	1	4 (3)	1''.2	H

Notes. Col. (1): total exposure time (s). The values for the sky frames are shown in parentheses. Col. (2): single-exposure time (s). Col. (3): number of coadd. Col. (4): total number of frames. Col.(5): C: cirrus, P: photometric, and H: high humidity. The values for the sky frames are shown in parentheses.

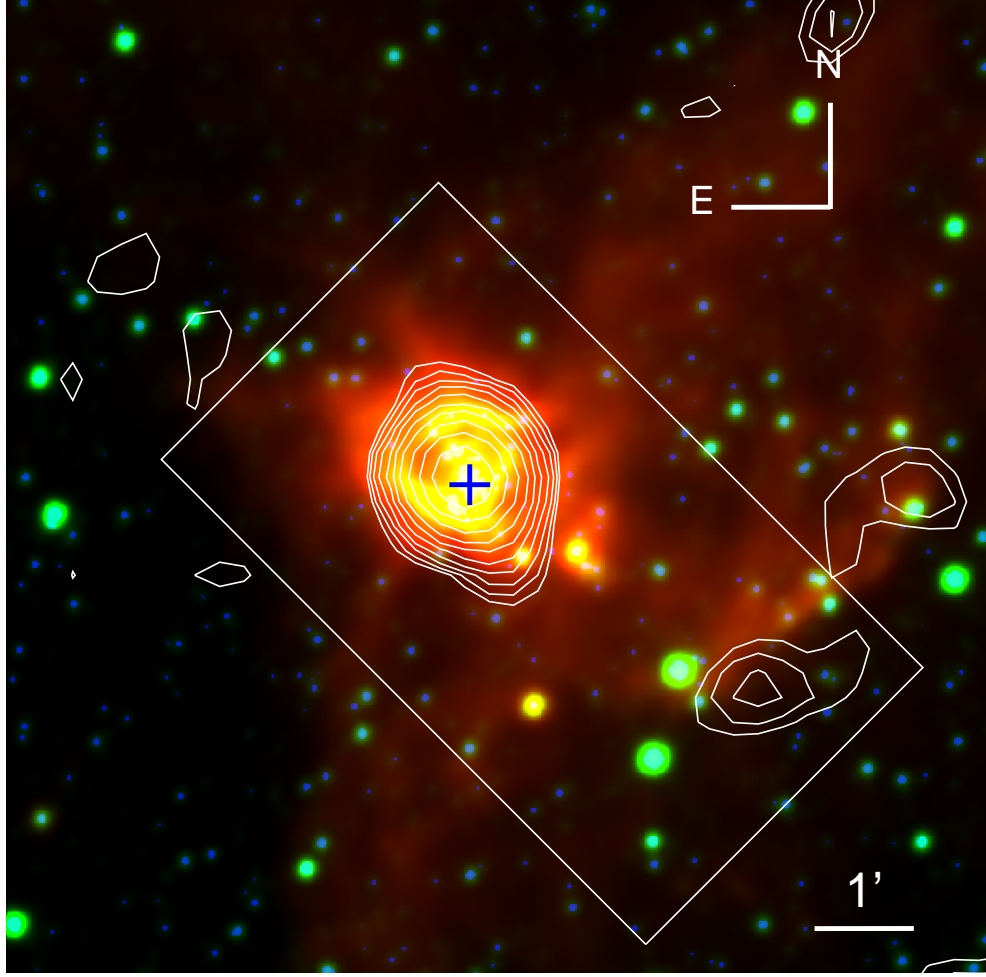


Figure 1. Pseudocolor image of S208 with the center of $(\alpha_{2000.0}, \delta_{2000.0}) = (04^{\text{h}}19^{\text{m}}32.92^{\text{s}}, +52^{\circ}58'41.6'')$ in Equatorial coordinates and $(l, b) = (151.2870^{\circ}, +1.9682^{\circ})$ in Galactic coordinates. The size of the field is $10' \times 10'$. North is up and east is to the left. The 1 arcmin corresponds to 2.7 pc and 1.2 pc for distances of S208 of 9 kpc and 4 kpc, respectively. The image is produced by combining the 2MASS K_S -band ($2.16 \mu\text{m}$; blue), *WISE* band 1 ($3.4 \mu\text{m}$; green), and *WISE* band 3 ($12 \mu\text{m}$; red). The 1.4 GHz radio continuum emission by NVSS is also shown using the white contours. The contours are plotted at $1 \text{ mJy beam}^{-1} \times 2^0, 2^{-1/2}, 2^1, \dots$. The blue plus symbol shows the brightest star in the optical bands (GSC 03719-00517). The white box shows the location and size of the MOIRCS field of view.

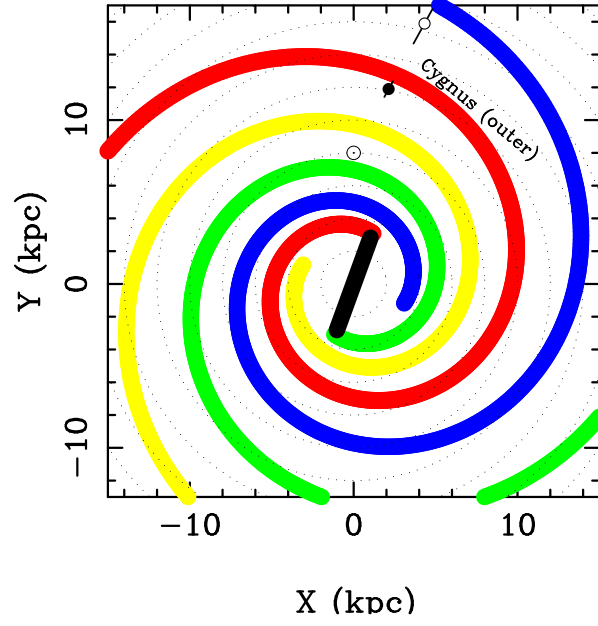


Figure 2. Top view of the Milky Way Galaxy, with S208 and spiral arms. S208 is shown with an open circle in the case of photometric distance and a filled circle in the case of kinematic distance. The photometric distance is based on all the derivations in Section 2.1, $D \sim 9$ kpc (7.6–10 kpc), while the kinematic distance is based on most recent derivation by Foster & Brunt (2015), $D = 4.4$ kpc with an uncertainty of 0.55 kpc, covering all the previous derivations in Section 2.1. The spiral arms from Vallée (2005), which are shown with different colors: red, yellow, green, and blue for Norma–Cygnus (outer) arm, Perseus arm, Sagittarius–Carina arm, and Scutum–Crux arm, respectively. The Sun is shown by a circled dot assuming the Galactocentric distance of 8.0 kpc. Dots show concentric circles around the Galactic center at a Galactic radius $r = 2, 4, 6, \dots, 22$ kpc.



Figure 3. JHK_S pseudocolor image of S208. The color image is produced by combining the J - ($1.26\ \mu\text{m}$), H - ($1.64\ \mu\text{m}$), and K_S -band ($2.15\ \mu\text{m}$) images obtained with MOIRCS at the Subaru telescope on 2008 January for J band and on 2007 November for H and K_S bands with the center of $\alpha_{2000} = 04^{\text{h}}19^{\text{m}}45^{\text{s}}$, $\delta_{2000} = +53^{\circ}05'41''$ in Equatorial coordinates. The field of view of the image is $\sim 7' \times 4'$, which is shown with a white box in Fig. 1. The yellow circle ($r = 35''$) shows the location of the cluster with the central coordinate of $\alpha_{2000} = 04^{\text{h}}19^{\text{m}}32.7^{\text{s}}$, $\delta_{2000} = +52^{\circ}58'34.6''$. The yellow dashed circle ($r = 15''$) shows the location of the small stellar association, which is identified by eye, with the central coordinate of $\alpha_{2000} = 04^{\text{h}}19^{\text{m}}24.6^{\text{s}}$, $\delta_{2000} = +52^{\circ}57'50.8''$.

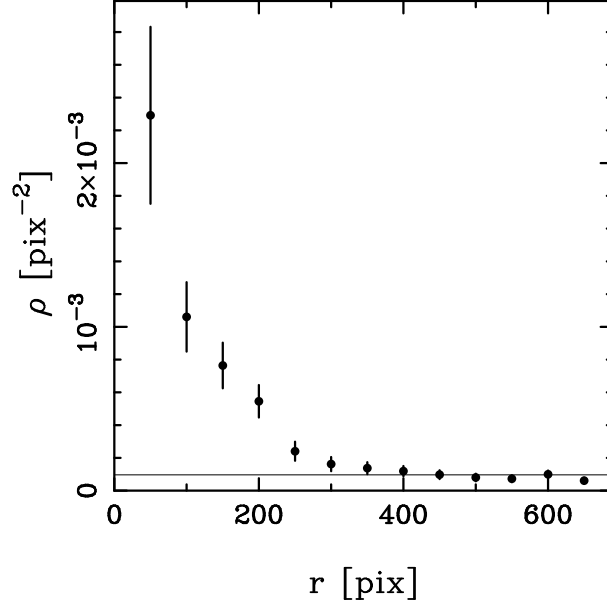


Figure 4. Radial variation of the projected stellar density of stars (filled circles) in the S208 cluster region with the center of $\alpha_{2000} = 04^{\text{h}}19^{\text{m}}32.7^{\text{s}}$, $\delta_{2000} = +52^{\circ}58'34.6''$. 50 pixels correspond to $\sim 6''$. The error bars represent Poisson errors. The horizontal solid line denotes the star density in the control field.

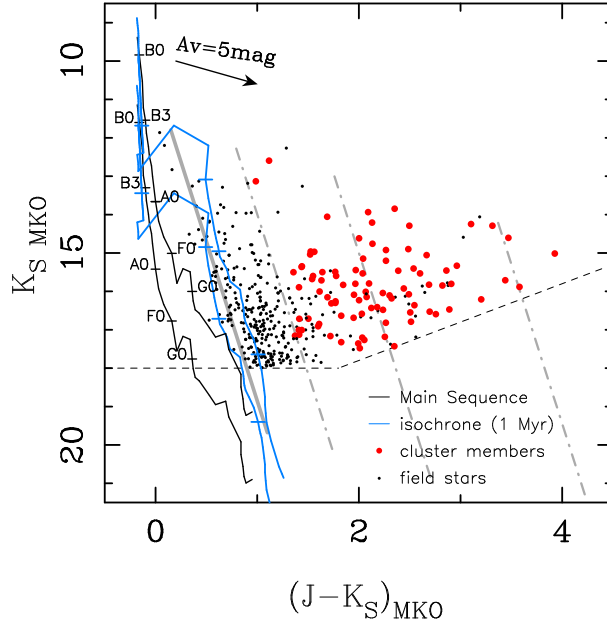


Figure 5. $(J - K_S)$ vs. K_S color-magnitude diagram of S208. Identified cluster members in the cluster region (yellow circle in Fig. 3) are shown with red filled circles, while other sources are shown with black dots. The arrow shows the reddening vector of $A_V = 5$ mag. The dashed lines mark the limiting magnitudes (10σ). The black lines show the dwarf tracks by Bessell & Brett (1988) in the spectral type of O9 to M6 (corresponding mass of ~ 0.1 – $20 M_{\odot}$). The blue line denotes the isochrone models for the age of 1 Myr old by D'Antona & Mazzitelli (1997, 1998; $0.017 \leq M/M_{\odot} \leq 3$), Siess et al. (2000; $3 < M/M_{\odot} \leq 7$), and Lejeune & Schaerer (2001; $7 < M/M_{\odot} \leq 40$). The distances of 9 kpc and 4 kpc are assumed. The short horizontal lines are placed on the isochrone models and are shown with the same colors as the isochrone tracks, which show the positions of 0.1, 1, 3, and $10 M_{\odot}$. For convenience, the isochrone models are approximated as straight lines, shown as the solid gray, for estimating the A_V value for each star. The dotted-dashed gray lines show the approximated isochrone models with extinctions of $A_V = 4, 10$, and 20 mag.

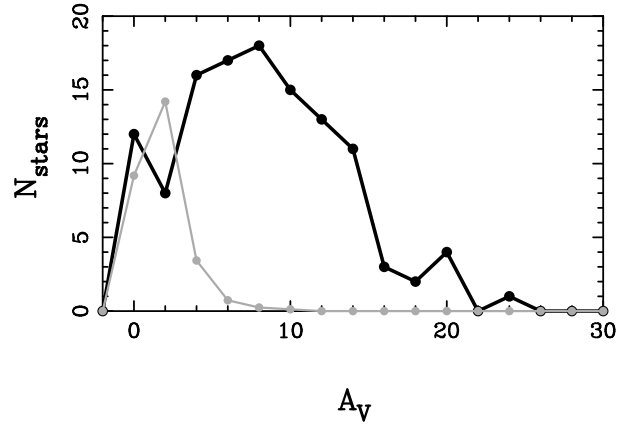


Figure 6. A_V distributions of stars in the S208 cluster region (black line) and stars in the control field (gray line). The distribution for the control field is normalized to match the total area of the cluster region.

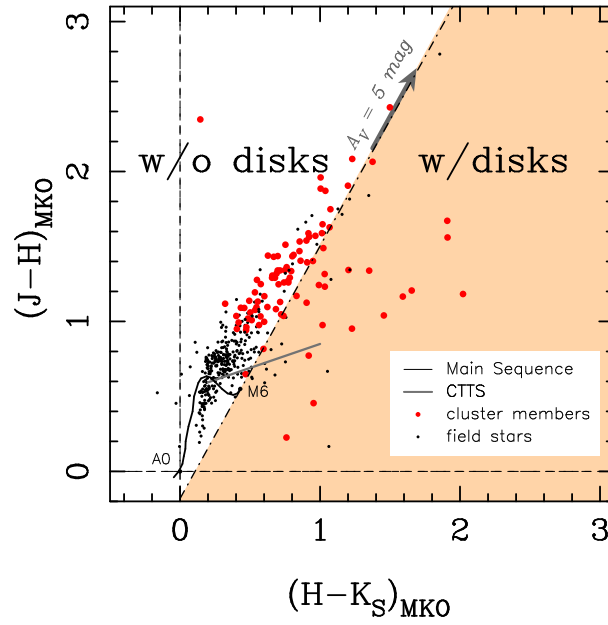


Figure 7. $(H-K_S)$ vs. $(J-H)$ color-color diagram of S208. Identified cluster members are shown as red filled circles, while all other stars in the S208 frame are shown as black dots. The solid curve in the lower left portion is the locus of the points corresponding to unreddened main-sequence stars. The dot-dashed line, which intersects the main-sequence curve at the maximum $H-K_S$ values (M6 point on the curve) and is parallel to the reddening vector, is the border between stars with and without circumstellar disks. The classical T Tauri star (CTTS) locus is shown with the gray line.

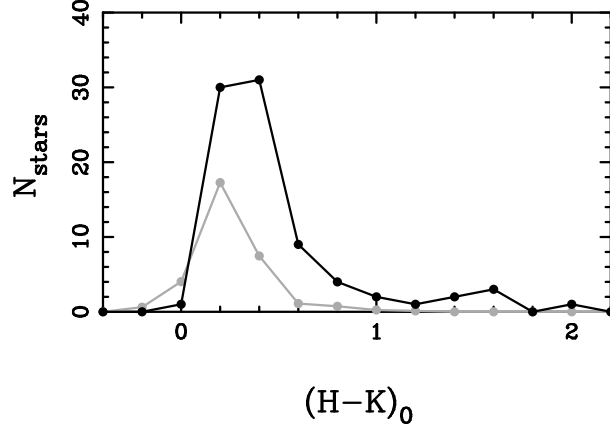


Figure 8. $(H-K)_0$ distributions for the S208 cluster members (black line) and stars in the control field (gray line). The distribution for the control field is normalized to match the total area of the cluster region.

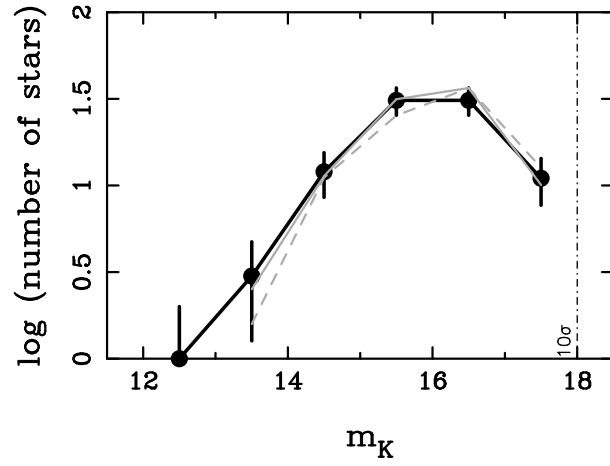


Figure 9. Raw KLFs for the S208 cluster members. The KLF for all the cluster members is shown by the black line with black dots ($A_V \geq 4$ mag). Error bars are the uncertainties from Poisson statistics. The KLFs for limited A_V samples are shown by gray lines, the gray solid line for the cluster members with A_V of 5–15 mag and the gray dashed line for the members with A_V of 6.2–13.0 mag. The gray solid line and gray dashed line are vertically shifted by +0.1 and +0.2, respectively. The vertical dotted-dashed line shows the limiting magnitudes of the 10σ detection (18.0 mag).

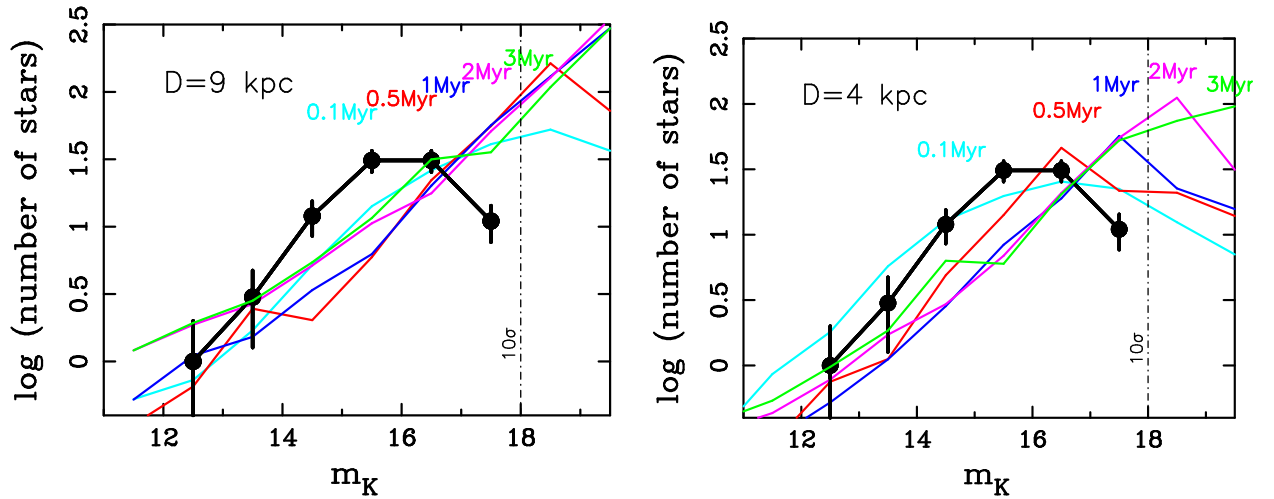


Figure 10. Comparison of the S208 KLFs (black lines) with model KLFs of various ages (colored lines). Error bars are the uncertainties from Poisson statistics. Two cases for the distance are assumed: photometric distance $D = 9$ kpc (left) and kinematic distance $D = 4$ kpc (right). The aqua, red, blue, magenta, and green lines represent model KLFs of 0.1, 0.5, 1, 2, and 3 Myr, respectively. The vertical dot-dashed lines show the limiting magnitudes of the 10σ detection (18.0 mag).

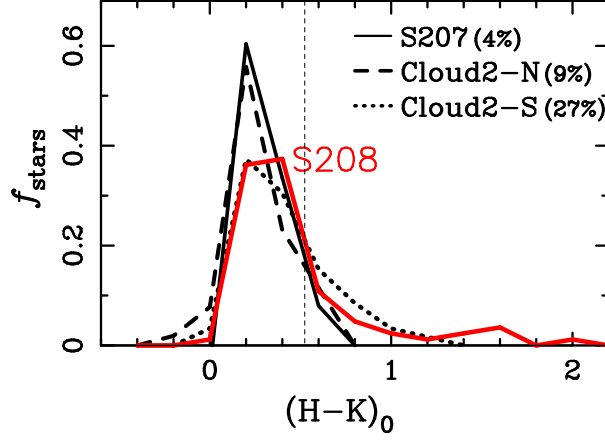


Figure 11. Comparison of intrinsic $H - K$ color distributions. The fractions of stars (f_{stars}) per each intrinsic color bin $(H - K)_0$ for clusters in low-metallicity environments, S208, S207, Cloud 2-N, and Cloud 2-S are plotted. The vertical dashed line shows the borderline for estimating the disk fraction in the MKO system.

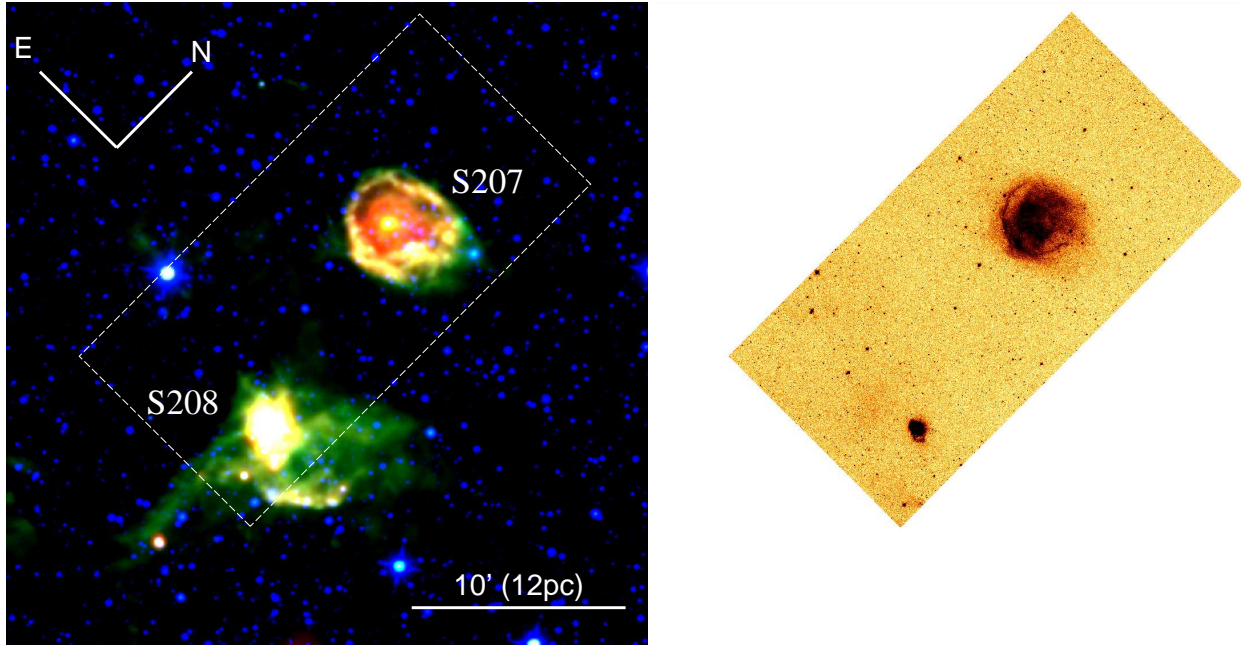


Figure 12. *Left:* *WISE* MIR pseudocolor image of S207 and S208 with a field of view ($30 \text{ arcmin} \times 30 \text{ arcmin}$) centered at $(l, b) = (151.24^\circ, +2.05^\circ)$ in Galactic coordinates. Galactic longitude is along the x-axis, while Galactic latitude is along the y-axis. The 10 arcmin corresponds to 12 pc for the distance of 4 kpc. The image is produced by combining *WISE* band 1 ($3.4 \mu\text{m}$; blue), *WISE* band 3 ($12 \mu\text{m}$; blue), and *WISE* band 4 ($22 \mu\text{m}$; red). *Right:* IPHAS $H\alpha$ image of S207 and S208 with the same scale as the left panel. The field of view is $\sim 11.3 \text{ arcmin} \times 22.6 \text{ arcmin}$, which is shown with a white dashed box in the left panel.

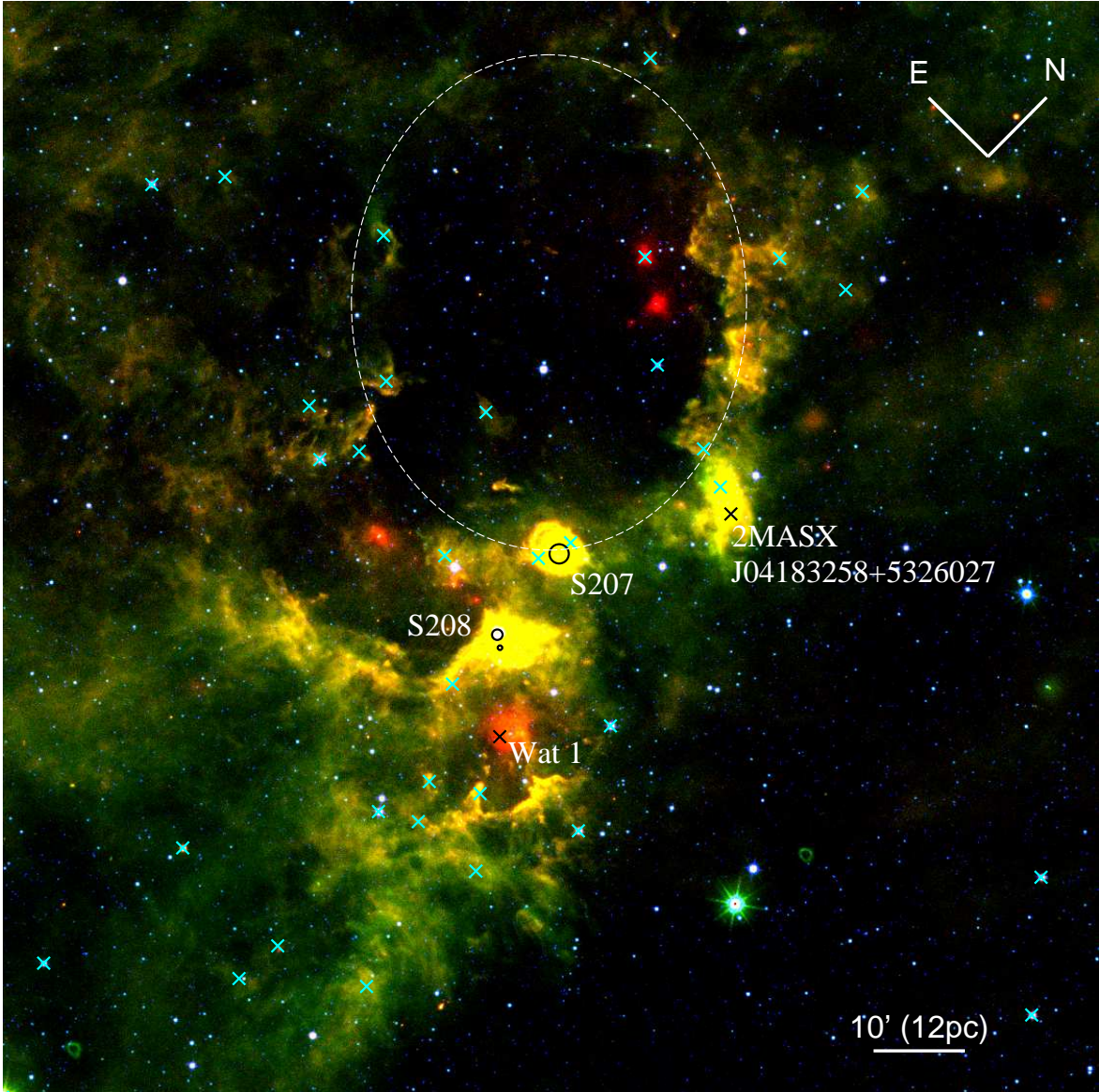


Figure 13. MIR pseudocolor image of S207 and S208 with a wide field of view ($2 \text{ deg} \times 2 \text{ deg}$) centered at $(l, b) = (151.19^\circ, +2.13^\circ)$ in Galactic coordinates. Galactic longitude is along the x-axis, while Galactic latitude is along the y-axis. The 10 arcmin corresponds to 12 pc for the distance of 4 kpc. The image is produced by combining the *WISE* band 1 ($3.4 \mu\text{m}$; blue), *WISE* band 3 ($12 \mu\text{m}$; blue), and *WISE* band 4 ($22 \mu\text{m}$; red). Black circles show the positions and sizes of the S207 cluster, the S208 cluster, and the S208 association. The cyan crosses show the locations of IRAS point sources, while the black crosses show other possible star-forming regions, 2MASX J04183258+5326027 and Waterloo 1 (Wat 1). White dashed ellipse shows the location of the bubble, which is identified by eye.